

© 2011 Thomas Casey Galvin

BOUND-FREE EMISSION AND ITS APPLICATION TO BROADBAND
OPTICAL AMPLIFIERS

BY

THOMAS CASEY GALVIN

THESIS

Submitted in partial fulfillment of the requirements
for the degree of Master of Science in Electrical and Computer Engineering
in the Graduate College of the
University of Illinois at Urbana-Champaign, 2011

Urbana, Illinois

Adviser:

Professor James Gary Eden

ABSTRACT

The potential for zinc and cadmium excimers to act as ultraviolet broad-band amplifier media is investigated. A detailed presentation of the theory of bound-free emission and free-bound absorption is given. New internuclear potential curves for the $B^1\Sigma_u^+$ upper states of both cadmium and zinc excimers are fit to observed data. Absorption, emission, and net gain spectra are calculated. Details of how to perform calculations are presented. The details of an ongoing experiment to demonstrate gain are presented.

ACKNOWLEDGMENTS

This project has been going on for much longer than I originally anticipated when it began. There are therefore many people to thank for their help. For efficiency, I have thanked people in table form, in the order in which they began helping me. By coin toss, family members have been thanked at the end.

Name	Thank you for...
Richard C. Muller	Countless hours of showing me math tricks Directing me toward engineering
Gary Eden	Introducing this project to me Supporting me during the project
Dr. CLARK WAGNER	Sharing his knowledge of vacuum systems Helping me revive the KrF
Scott McDonald	Help in constructing my first oven Building a second, much better oven
JD Readle	Early experimental and data taking help
Thomas Spinka	Creating the original spectral simulation code Helping to validate the code
Thomas ‘Sparkles’ Houlahan	Taking over my apprenticeship from Paul Putting up with my pranks
Darby Hewitt	Being my officemate General awesomeness Helping to play pranks on Sparkles
Kyle Raymond	Digitizing potentials
Mom and Dad	Reading to me when I was little Alligators My good looks
Chork and Krista	Stuff
Patreek	Deep fried goodness

TABLE OF CONTENTS

LIST OF ABBREVIATIONS	v
CHAPTER 1 INTRODUCTION	1
CHAPTER 2 THEORY	3
2.1 Atomic Considerations	3
2.2 Bound-Free Emission	3
2.3 Photoassociation	6
2.4 Semiclassical Interpretation	7
2.5 Femtosecond Lasers	10
2.6 Maximum Power Considerations	11
CHAPTER 3 CALCULATION OF BOUND-FREE EMISSION SPECTRA	13
3.1 Calculation of Emission Spectra	13
3.2 Calculation of Absorption Spectra	15
3.3 Net Gain Spectra	18
3.4 Validation	18
3.5 Optimization of Potentials	18
CHAPTER 4 EXPERIMENTS	25
4.1 Fluorescence Spectroscopy Experiments	25
4.2 Amplifier Experiments	28
CHAPTER 5 CONCLUSION AND FUTURE WORK	32
APPENDIX A SPECTRAL SIMULATION CODE	33
APPENDIX B THE NUMEROV METHOD	34
REFERENCES	36

LIST OF ABBREVIATIONS

ASE	Amplified Stimulated Emission
BBO	Beta Barium Borate
FCF	Franck-Condon Factor
FROG	Frequency Resolved Optical Grating
IR	Infrared
OPA	Optical Parametric Amplifier
SPM	Self-Phase Modulation
UV	Ultraviolet

CHAPTER 1

INTRODUCTION

Bound-free emission from optically pumped zinc and cadmium dimers presents an opportunity to create higher peak intensity ultraviolet (UV) pulses than has been previously possible. In this thesis, the theory of bound-free emission will be explained and experiments directed at demonstrating gain will be presented.

The strong focusability of lasers in the UV allows extremely high optical intensities to be reached. Picosecond UV pulses were used by C. K. Rhodes in his original study of high-order optical nonlinearities. Intensities of up to 10^{17} W/cm² were generated by focusing high-quality 193 nm pulses [1]. Ultraviolet radiation has been found to couple more efficiently to plasmas than light of longer wavelengths. Plasmas heated by UV laser radiation can be generated with electron temperatures of up to 8 keV. Such plasmas have applications in high harmonic generation, x-ray lasers, and perhaps even fusion research [2]. Finally, the ability to deposit energy quickly at ultraviolet wavelengths has applications in micromachining [3].

High-powered ultrafast (sub-picosecond) lasers have been available in the visible and infrared for some time, but relatively few such sources exist in the ultraviolet. The bound-free emission of Zn₂ and Cd₂ excimers may offer a new method of amplifying ultrafast pulses in the ultraviolet. The broad bandwidth of those transitions may allow the creation of pulses shorter than have ever been seen in the ultraviolet region at high power.

There has been interest in optically pumping bound-free transitions to create a tunable laser since the 1970's. Smith et al. presented a theoretical analysis of absorption, fluorescence, and stimulated emission in a Hg₂ laser [4]. Discharge pumped excimer lasers based on the rare gas halides (ArF, KrF, XeCL, etc.) have already been shown to amplify femtosecond pulses. The author knows of no attempts to amplify femtosecond pulses in metallic vapors, such as Cd₂ and Zn₂; but because they are chemically similar to the

rare gas halides, there is reason to believe that amplification of UV fs pulses will be possible.

As mentioned above, several excimer systems have already been used to amplify ultrafast pulses successfully. High-energy ultrafast pulses were generated in the visible and frequency doubled into the UV. This light is then passed through an excimer plasma. Krypton fluoride lasers have been shown to be the most efficient with this technique. Up to 200 mJ pulses have been generated; and in a separate experiment, Szatmari was able to obtain amplified pulses as short as 45 fs, limited by the gain bandwidth of the KrF transition. This bandwidth is approximately 0.5 nm [3]. The gain bandwidth of the $B^1\Sigma_u^+ \rightarrow X^1\Sigma_g^+$ transition in Zn_2 and Cd_2 is at least six times that for the KrF transition.

Excimer technology is not the only technology for broadband UV amplification. Several solid state amplifying media have been developed, most notably Ce:LiSAF and Ce:LiCAF. These crystals have been developed both as stand-alone oscillators and as injection seeded amplifiers. The amplifiers have been shown to have a pulsed output energy in the 1 mJ range, though this is for a pulse lasting several nanoseconds. The peak energies are limited by the damage threshold of the crystal [5, 6].

CHAPTER 2

THEORY

2.1 Atomic Considerations

Both atomic zinc and cadmium have 1S_0 ground states. This means that the atomic subshells are filled. The diatomic ground states are therefore generally dissociative. The only attractive force is a weak van der Waals interaction. The $B^1\Sigma_u^+$ upper states of zinc and cadmium dimers are both formed by 1S_0 and 1P_0 atomic states. This state is bound by approximately 1 eV in both cases.

2.2 Bound-Free Emission

Understanding the unusual nature of bound-free emission is key to understanding the large gain bandwidth that excimer lasers provide. Bound-free transitions can be understood in the context of the theory of diatomic molecules, which will be discussed presently. Neglecting relativistic effects, the Hamiltonian for any diatomic molecule can be written as

$$\begin{aligned} \hat{H} = & -\frac{\hbar^2}{2M_A}\nabla_A^2 - \frac{\hbar^2}{2M_B}\nabla_B^2 - \frac{\hbar^2}{2m_e}\sum_i\nabla_i^2 + \\ & \frac{e^2}{4\pi\epsilon_0}\left(\frac{Z_A Z_B}{r_{AB}} + \sum_i\sum_{j>i}\frac{1}{r_{ij}} - \sum_i\frac{Z_A}{r_{Ai}} - \sum_i\frac{Z_B}{r_{Bi}}\right) \end{aligned} \quad (2.1)$$

where the M_i 's are the masses of the nuclei, m_e is the electron mass, the Z_i 's are the atomic charges, and the r_{ij} 's are the distances between particles i and j . The sums over i and j are performed over all electrons.

For diatomic molecules with many electrons, solving the eigenequation with Equation 2.1 is clearly intractable without making approximations. In

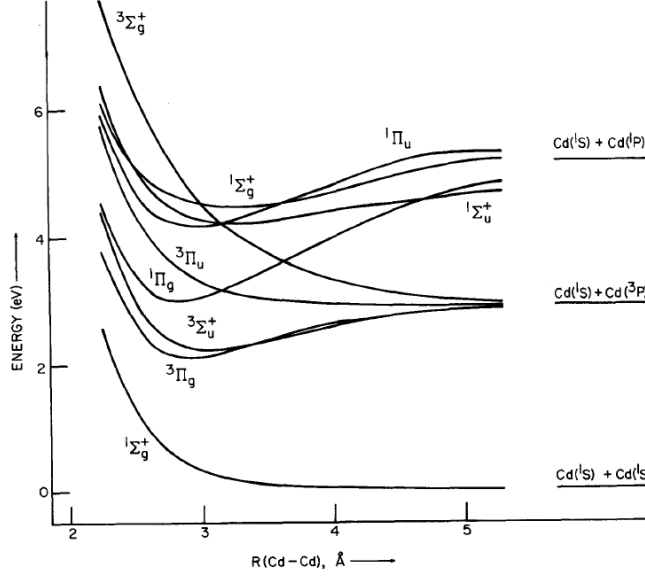


Figure 2.1: Potential curves of cadmium. Curves produced by *ab initio* calculations performed by Bender et al. [7].

even the lightest molecules, each nucleus is more than 1800 times more massive than an electron. The nuclei therefore respond to forces much more slowly than electrons. If the electrons are assumed to respond instantaneously to changes in nuclear position, the motion of the electrons and nuclei can be decoupled. For every internuclear separation r , the electrons arrange themselves in an eigenstate of the potential generated by the nuclei at that separation. The eigenstate energy of the electrons can then be included with the Coulomb potential between the two nuclei in an effective potential $V(r)$. This is the well-known Born-Oppenheimer approximation, which is the starting point of quantum chemistry. It justifies our use of potentials such as presented in Figure 2.1.

The potential of the nuclei being separated by a distance r can be found either by performing *ab initio* quantum calculations or fitting potentials to empirical data. *Ab initio* calculations are difficult and consume large amounts of processing power. The potentials used in the simulations in this thesis were inferred from spectroscopic and scattering experiments. Once the potential functions have been found, the Schrodinger equation for the two nuclei can be written as

$$\left[\frac{-\hbar^2}{2M_A} \nabla_A^2 + \frac{-\hbar^2}{2M_B} \nabla_B^2 + V(r) \right] \Psi = E\Psi \quad (2.2)$$

where ∇_A and ∇_B operate only on their respective coordinates. Recall that $V(r)$ contains both the energy from the coulombic interaction of the two nuclei and a term for the energy of the electron eigenenergies in the potential field of the nuclei being separated by a distance r . By using the substitutions $R = M_A r_A + M_B + r_B$ and $r = r_B - r_A$, Equation 2.2 can be converted to center of mass coordinates. Ignoring the equation describing the center of mass, we have

$$\left(\frac{-\hbar^2}{2\mu} \nabla^2 + V(r) \right) \Psi = E\Psi \quad (2.3)$$

The quantity μ is the reduced mass of the molecule. The standard technique of solving Equation 2.3 is to convert it into spherical coordinates. Because the potential is a function of r alone, it is possible to write $\Psi(r, \phi, \theta) = R(r)\Phi(\phi)\Theta(\theta)$. This is the separation of variables technique. The solutions for $\Phi(\phi)\Theta(\theta)$ are the spherical harmonics. Meanwhile, the radial equation is

$$\frac{-\hbar^2}{2\mu} \frac{d^2}{dr^2} R(r) + \left[V(r) + \frac{\hbar^2}{2\mu r^2} J(J+1) \right] R(r) = ER(r) \quad (2.4)$$

where the r^{-2} term added to the potential is due to the rotational motion. For heavier molecules, the rotational term is less important and is often ignored. The equation can then be solved numerically to determine the eigenenergies and wavefunctions. Solutions with $E > 0$ are unbound wavefunctions; solutions with $E < 0$ are bound wavefunctions. In actual molecules, the potential well is finite and thus there will be a finite number of bound states.

With the wavefunctions and energies in hand, the relative intensity of emission at each wavelength can be calculated using the Franck-Condon principle. This principle states that because the nuclei are much more massive than the electrons, nuclear position and momenta are approximately conserved during an electronic transition. Nuclear position is conserved because the electronic structure changes so rapidly that the nuclei cannot move significantly in the time it takes for an electronic transition to occur. The conservation of position leads to vertical transitions on plots like that of Figure 2.2. The conservation of momentum occurs because any changes in the electron momentum are insignificant compared to the momentum of the nuclei. Because nuclear momentum is conserved during a transition, kinetic energy must be conserved. In Figure 2.2, this requirement causes transitions to terminate on the dashed line, where the kinetic energy of the lower state is the same as

the kinetic energy of the upper state. This will be discussed further in the next section.

The Franck-Condon principle is expressed mathematically as

$$FC_{\nu',J,\epsilon''} = \left| \int \psi_{\nu',J}^*(r) \mu_e(r) \psi_{\epsilon''}(r) dr \right|^2 \quad (2.5)$$

where $\mu_e(r)$ is the dipole moment operator. This term arises from the overlap of the electronic wavefunctions of the upper and lower states. In general, it is a function of position; but in cases where $\mu(r)$ is not known, it is generally treated as a constant.

The contribution to the spectrum from a pair of upper and lower states, known as a partial wave, is expressed as

$$P_{\nu',J}(\nu) = (2J+1) \sqrt{\frac{\mu}{\hbar^2 \pi^2 E''}} FC_{\nu',J,\epsilon''} \delta(E' - E'' - \nu) \quad (2.6)$$

which can be recognized as Fermi's Golden Rule. The first two terms are the density of states for the lower state. The Franck-Condon factor is the oscillator strength while the last term is for energy conservation.

It is necessary to sum over a large number of upper and lower states to find all contributions to the spectrum. The result is known as the lineshape function

$$S(\nu) = \sum_{\nu',J} C_{\nu',J} P_{\nu',J}(\nu) \quad (2.7)$$

where the $C_{\nu',J}$ term is the relative population of the ν', J state.

The above quantity gives the relative intensities of photon emission, but spectrometers are typically calibrated to detect intensity, not photon number. To convert to intensity, the lineshape function is multiplied by photon energy. The result is

$$I(\nu) \propto \nu S(\nu) \quad (2.8)$$

2.3 Photoassociation

Photoassociation (free-bound absorption) is the inverse process of bound-free emission. Unsurprisingly then, the photoassociation can be analyzed using very similar equations. The only difference is that the $C_{\nu',J}$ factor in

Equation 2.6 is replaced by a Boltzmann factor. Thus

$$P_{\nu',J}(\nu) = (2J+1) \exp\left(\frac{-\epsilon''}{k_B T}\right) \sqrt{\frac{\mu}{\hbar^2 \pi^2 E''}} F C_{\nu',J,\epsilon''} \delta(E' - E'' - \nu) \quad (2.9)$$

where k_B is Boltzmann's constant.

Finally, the net absorption coefficient is

$$\alpha(\nu) = \frac{8\pi^3}{3\lambda} e^2 a_0^2 \frac{1}{g_e Q_t} S(\nu) [N]^2 \quad (2.10)$$

where a_0 is the Bohr radius, $[N]$ is the density of free atoms, and g_e and Q_t are the electronic and vibrational partition functions, respectively.

2.4 Semiclassical Interpretation

The quantum picture presented in the last section correctly predicts spectra but fails to give an intuitive understanding of the physics. For this purpose a semiclassical picture of how the Franck-Condon principle relates to bound-free emission will now be presented. This picture was originally described by Tellinghuisen [8]. The potentials of the nuclei, including the electronic energy contributions, are assumed known. They are denoted by $V'(r)$ for the upper state and $V''(r)$ for the lower state. The upper state is assumed to be bound with discrete vibrational energy levels indexed by ν' . The lower state is assumed to be dissociative. The free wavefunctions are labelled by their energy ϵ'' . The upper and lower state wavefunctions can be found using the WKB approximation

$$\psi_{\nu'} = k_{\nu'}^{-1/2} \cos(\phi_{\nu'}) \quad (2.11)$$

$$\psi_{\epsilon} = k_{\epsilon''}^{-1/2} \cos(\phi_{\epsilon''}) \quad (2.12)$$

where

$$k_{\epsilon''}^2 = \frac{2\mu}{\hbar^2} [\epsilon'' - V''(R)] \quad (2.13)$$

$$\phi_{\epsilon''} = \int_{R''}^{R^*} k_{\epsilon''} dR - \frac{\pi}{4} \quad (2.14)$$

and \hbar and μ are the reduced Planck's constant and the reduced mass, respectively. The quantities $k_{\nu'}$ and $\phi_{\nu'}$ are defined similarly.

The Franck-Condon overlap integral is then

$$\begin{aligned}\langle \epsilon'' | \mu_e(R) | \nu' \rangle &\approx \int (k_{\epsilon''} k_{\nu'})^{-1/2} \mu_e(R) \cos(\phi_{\nu'}) \cos(\phi_{\epsilon''}) dR \\ &= \frac{1}{2} \int (k_{\epsilon''} k_{\nu'})^{-1/2} \mu_e(R) [\cos(\phi_{\nu'} + \phi_{\epsilon''}) \\ &\quad + \cos(\phi_{\nu'} - \phi_{\epsilon''})] dR\end{aligned}\tag{2.15}$$

The last integral in Equation 2.15 can be evaluated by the method of stationary phase. This principle states that if k is large, then the integral can accumulate appreciably only where

$$\frac{\partial}{\partial R}(\phi_{\nu'} \pm \phi_{\epsilon''}) = k_{\epsilon''} \pm k_{\nu'} = 0\tag{2.16}$$

The plus term has no solution; however, the minus term leads directly to

$$\epsilon'' - V''(r) = E_{\nu'} - V'(r)\tag{2.17}$$

This is precisely the conservation of nuclear momentum deduced earlier. Stated another way, strong coupling between a given upper vibrational state and lower free state at a given r occurs only when the lower state has energy

$$\epsilon'' = E_{\nu'} + V''(r) - V'(r)\tag{2.18}$$

This curve is known as the difference potential.

This semiclassical theory allows us to see trends in bound-free emission and free-bound absorption (photoassociation). The upper and lower states of the zinc transition used in our experiment are shown in Figure 2.2. All of the following discussion focuses on these potential curves and the similarly shaped potentials for cadmium. The conclusions drawn here will in general describe systems with weakly bound or unbound lower states and bound upper states.

Photons are most efficiently absorbed into a given vibrational level through transitions near the right-hand terminus of the classically allowed region [9]. This region is generally the most thermally accessible portion of the lower state energy potential. Absorption from the weakly bound ground

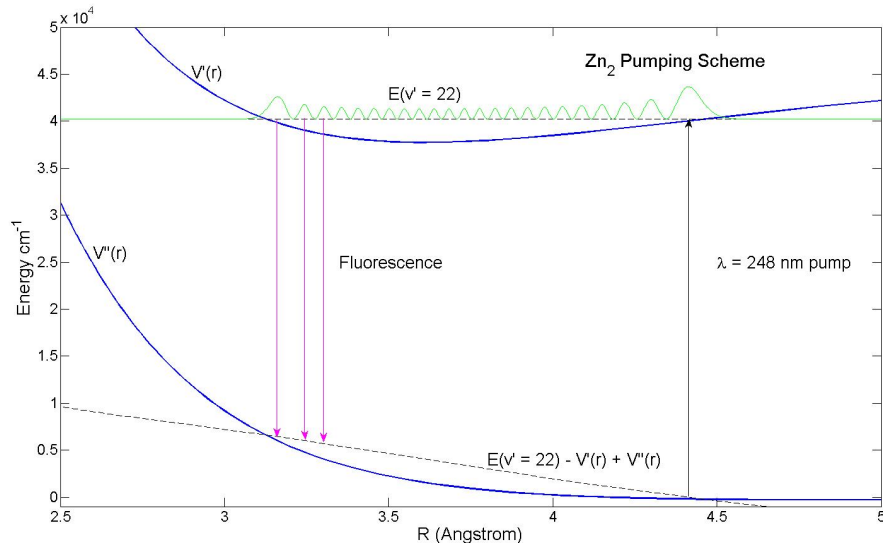


Figure 2.2: Photons are absorbed near the outer classical turning point of the upper state, where the difference potential $E(\nu' = 22) - V'(r) + V''(r)$ is thermally accessible. Excited molecules may radiate at any internuclear separation with nonzero probability amplitude. Arrows representing the three longest-wavelength peaks of the emission spectrum have been drawn.

state is generally unimportant because $kT \sim D_e$ at the temperatures of our experiment, and the degeneracy of the free states is significantly greater than that of the bound states. Hence very few atoms will exist in molecules at thermal equilibrium.

After the molecule is formed by the absorption of a photon, the molecule decays back to its ground state by spontaneously emitting a photon. The probability of the molecule radiating from a given internuclear separation is proportional to the amplitude squared of the vibrational wavefunction at that separation. Radiative transitions must terminate on the difference potential, which varies with internuclear separation. If the difference potential is strictly decreasing, photons emitted from two different internuclear separations will have different energies. Together, these facts imply that each peak of the vibrational wavefunction corresponds to a peak in the emission spectrum.

The overall bandwidth of the observed fluorescences is determined primarily by the slope of the lower state potential in the classically allowed region of the upper state. The difference between the maximum and minimum of the difference potential defines the energy range of allowed transitions, and

hence the bandwidth of the transition. If the lower potential were flat, for example, then the difference potential would be an upside-down portion of the upper state potential function. The height of the vibrational level over the minimum of the potential would then be equal to the energy bandwidth of the transition. Alternatively, if the classically allowed region of the upper state coincided with the repulsive core of the lower state, the bandwidth would be significant.

When the upper state of a bound-free transition is excited collisionally (in an electric discharge, for example), Condon interference is not typically observed [9] because many upper state vibrational levels are inevitably excited. The interference patterns from different vibrational levels overlap each other, producing an unstructured continuum from which it is impossible to gain information about the radial potentials. Filling in the spectrum may in fact be useful for increasing the bandwidth of a laser amplifier.

2.5 Femtosecond Lasers

Femtosecond pulses are generated by the technique of modelocking. In this method, the longitudinal cavity modes are forced to oscillate coherently, interfering constructively for only a short time. To implement this idea, a medium with a large gain bandwidth (Ti:Sapphire in this experiment) is placed in a macroscopic cavity. Normal laser cavities are dispersive; that is, they have a different optical length for different wavelengths. This cannot be allowed in modelocked operation, because after one round trip, the relative phases of the various modes would have changed. In order to maintain the various modes in phase, the net cavity dispersion must be kept at zero. This is accomplished using chirped mirrors and tuning prisms in the cavity to correct for the second and third order dispersion. To lock the phases together, an element is introduced into the cavity which has intensity-dependent loss. This will favor the modes constructively interfering.

Some experiments require a higher peak power than femtosecond oscillators are capable of providing. The most common arrangement for generating high-powered femtosecond pulses is chirped pulse amplification. Direct amplification of a femtosecond beam is difficult because the high peak intensities can damage optical coatings as well as cause nonlinear effects in the materials

they pass through. To get around this problem, the pulses are temporally stretched. Polarization-dependent optical switches then trap the pulse inside another cavity containing a region of high gain. When the pulse has saturated the gain medium, it is ejected from the cavity. The pulse is then temporally recompressed.

As is well known, the Einstein A coefficient can be expressed as

$$A = \frac{\nu^3 |r|^2}{24\pi^4 \epsilon_0 \hbar c^3} \quad (2.19)$$

where r is the dipole moment. The spontaneous emission rate increases as the cube of the frequency. Because the upper state lifetime is proportional to $1/A$, energy storage is limited at high frequencies. Now consider the standard relationship between the Einstein A and B coefficients

$$A \propto B\nu^3 \quad (2.20)$$

Equation 2.20 states the likelihood of an atom to spontaneously radiate its energy away rather than emit coherently with the field scales as the frequency cubed. Hence, spontaneous emission becomes a problem at higher frequencies, creating a two-fold problem: First, the laser will need to be pumped harder because so much energy is going into spontaneous emission; second, spontaneous emission is noise, which will limit our ability to temporally compress the pulses [3]. Hence it would be difficult to create an ultraviolet femtosecond oscillator.

Saturable absorbers, chirped mirrors, and other modelocking technologies are well developed in the IR, but do not exist in the ultraviolet. Nonlinear techniques have been developed to change the center wavelength of femtosecond pulses. A two-wavelength system where femtosecond pulses are generated in the IR and amplified in the UV offers several advantages over directly generating femtosecond pulses in the UV.

2.6 Maximum Power Considerations

It is now wise to consider how much power could be extracted from an amplifier based on an ultraviolet excimer transition. The general formula for

saturation intensity is

$$I_{sat} = \frac{h\nu}{\sigma\tau_2} \quad (2.21)$$

where $h\nu$ is the photon energy, σ is the stimulated emission cross section, and τ_2 is the upper state lifetime. This quantity is generally large because the transition is in the UV and the lifetime of the upper state is extremely short. After the excimer molecule radiates to its ground state, the two atoms have significant momentum relative to each other. The molecule will quickly dissociate (on the order of femtoseconds) and the two atoms will have inelastic collisions with other atoms and thermalize. The maximum power this system is capable of delivering will not be limited by the saturation intensity of the transition or the lifetime of the lower state.

One of several other factors will limit the power available from an amplifier constructed with zinc and cadmium dimers. First, the power will be limited to the energy that can be pumped into the upper state by the KrF laser. At high enough intensities, nonlinear effects will emerge. Some of them, such as self-focusing and self-phase modulation can ruin the quality of the beam. A heavily pumped system may suffer from excited state absorption. The energy levels of Zn_2 and Cd_2 lying 5 eV above the excited state have not been mapped.

CHAPTER 3

CALCULATION OF BOUND-FREE EMISSION SPECTRA

The previous chapter discussed the theory of how spectra can be calculated from interatomic potentials. This chapter will detail how to actually perform these calculations. The actual code used in this thesis is available (see Appendix A). Here, the specific example of bound-free emission and free-bound absorption (photoassociation) will be discussed; but the extension of these ideas to bound-bound, free-bound, and free-free transitions should be obvious.

3.1 Calculation of Emission Spectra

The following describes how to calculate a relative emission spectrum from a single upper state vibrational level. This task can be divided into three parts: calculation of the wavefunctions, calculation of the partial waves, and finally mapping those partial waves onto spectra.

Because there is not an analytic expression for the wavefunctions of the upper and lower states, they must be computed numerically. In order to make this possible, the internuclear spacing must be limited to a finite interval and quantized. The internuclear separation interval for the upper state must contain the entire classically allowed region and enough of the classically forbidden region so that the amplitude of the highest vibrational level of interest is negligibly small at the ends of the interval. The interval for the lower states must also contain enough of the classically forbidden region so that the wavefunction is negligibly small. Due to the way in which the lower state wavefunction needs to be normalized (see below), the interval for the lower state must extend to the dissociated limit. The step size can be determined by steadily decreasing it until it has no apparent effect on the wavefunctions.

While the bound upper state wavefunctions have discrete energies, the lower state wavefunctions may have any energy in a continuum. In order to calculate spectra, the energies are sampled. The energy spacing between samples must be smaller than any spectral feature of the transition. The lower limit of energies should be slightly above the dissociative limit. The upper limit on energies can be set by looking at where the Franck-Condon factors above the maximum energy are essentially zero, which can be predicted by looking at the difference potential.

The lower state wavefunctions are calculated via the Numerov method (see Appendix B). In order to account for the density of states term in Equation 2.6, the functions are normalized so that their amplitude squared in the dissociative limit is

$$\frac{1}{\sqrt{E}} \quad (3.1)$$

where the zero of energy is defined as the dissociated limit of the atoms. Note that as compared to Equation 2.6, all constants of proportionality have been discarded. Only the relative intensity of emission is being calculated. Calculation of absolute spectra would require knowledge of the dipole moment operator, which is not available.

Looking at Equation 2.4, it can be seen that the Hamiltonian for this system can relatively easily be expressed in the position basis. The second derivative can be approximated by

$$\psi''(r_n) \approx \frac{\psi(r_{n+1}) - 2\psi(r_n) + \psi(r_{n-1}))}{h^2} \quad (3.2)$$

A matrix form of the Hamiltonian is then

$$\hat{H} = \begin{bmatrix} V(r_1) + \frac{\hbar^2}{\mu} & -\frac{\hbar^2}{2\mu} & & \dots \\ -\frac{\hbar^2}{2\mu} & V(r_2) + \frac{\hbar^2}{\mu} & -\frac{\hbar^2}{2\mu} & \\ & -\frac{\hbar^2}{2\mu} & V(r_3) + \frac{\hbar^2}{\mu} & \\ \vdots & & & \ddots \end{bmatrix} \quad (3.3)$$

An eigenvector solver can then be used to find the wavefunctions. All wavefunctions were normalized so that their integrated magnitude squared was unity.

With the wavefunctions for the upper and lower states in hand, the next step is to calculate the partial wave factors. This task can be accomplished

by taking an inner product between the upper and lower wavefunctions as in Equation 2.5. Recall that the density of states is included in the normalization of the lower state wavefunctions.

Each partial wave is mapped onto a wavelength based on the energy difference between the upper and lower states. These factors are accumulated in a vector where each element represents the relative intensity of emission at a given wavelength.

To simulate the effect of a finite resolution spectrometer, the line spectrum is then convolved with a lorentzian function. To ensure accuracy, care must be taken that the line spectrum is zero at the edges of its range. Note that it is not possible to simulate an arbitrary resolution spectrometer with a fixed lower state energy sampling. The uniform sampling of lower state energies introduces artificial structure into the spectrum. This structure will be washed out if the width of the lorentzian function is much greater than the energy sampling interval of the lower states.

3.2 Calculation of Absorption Spectra

Calculation of the absorption spectrum is nearly identical to calculation of emission spectrum. The relative weighting of the partial waves in Equation 2.6 are replaced with the Boltzmann factors for the lower state energies as in Equation 2.9.

Plots of the calculated absorption spectra for both cadmium and zinc is shown in Figure 3.1. Note that the absorption spectra do not share the highly structured properties as bound-free emission from a single vibrational level of the upper state. While absorption into a single state would show the perfectly modulated structure, absorption into multiple levels washes out the interference terms. Figure 3.2 gives another image of this behavior. Here the relative absorption into a particular level is plotted against pumping wavelength.

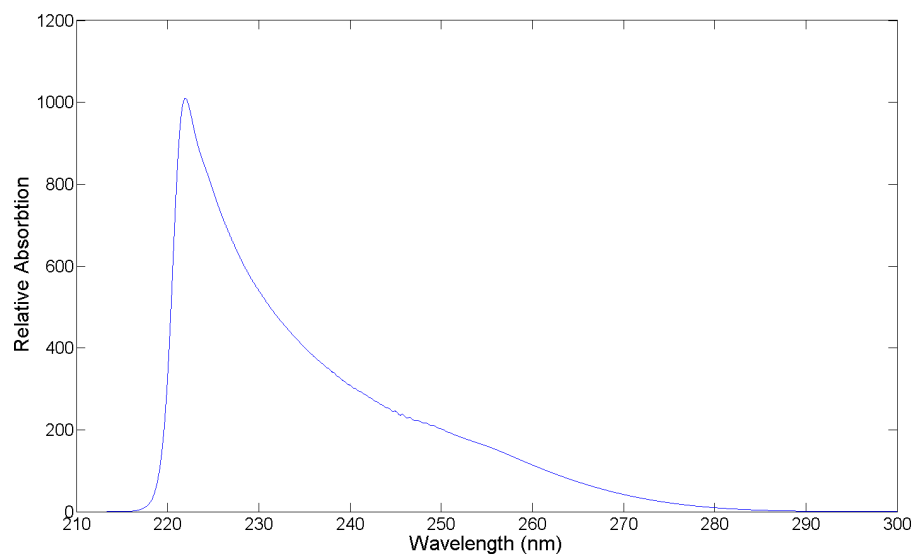
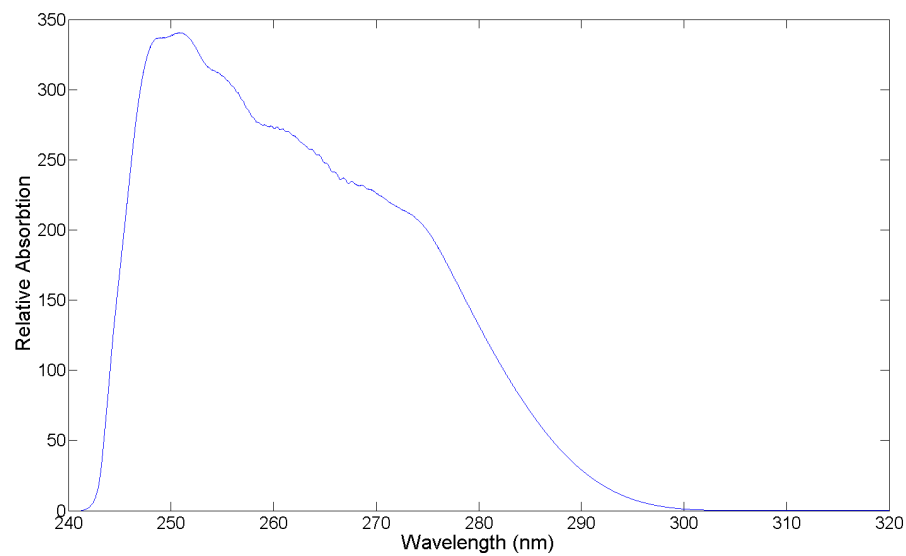


Figure 3.1: Absorption due to photoassociation in cadmium (top) at 982 K and zinc (bottom) at 1118 K (both at 400 torr).

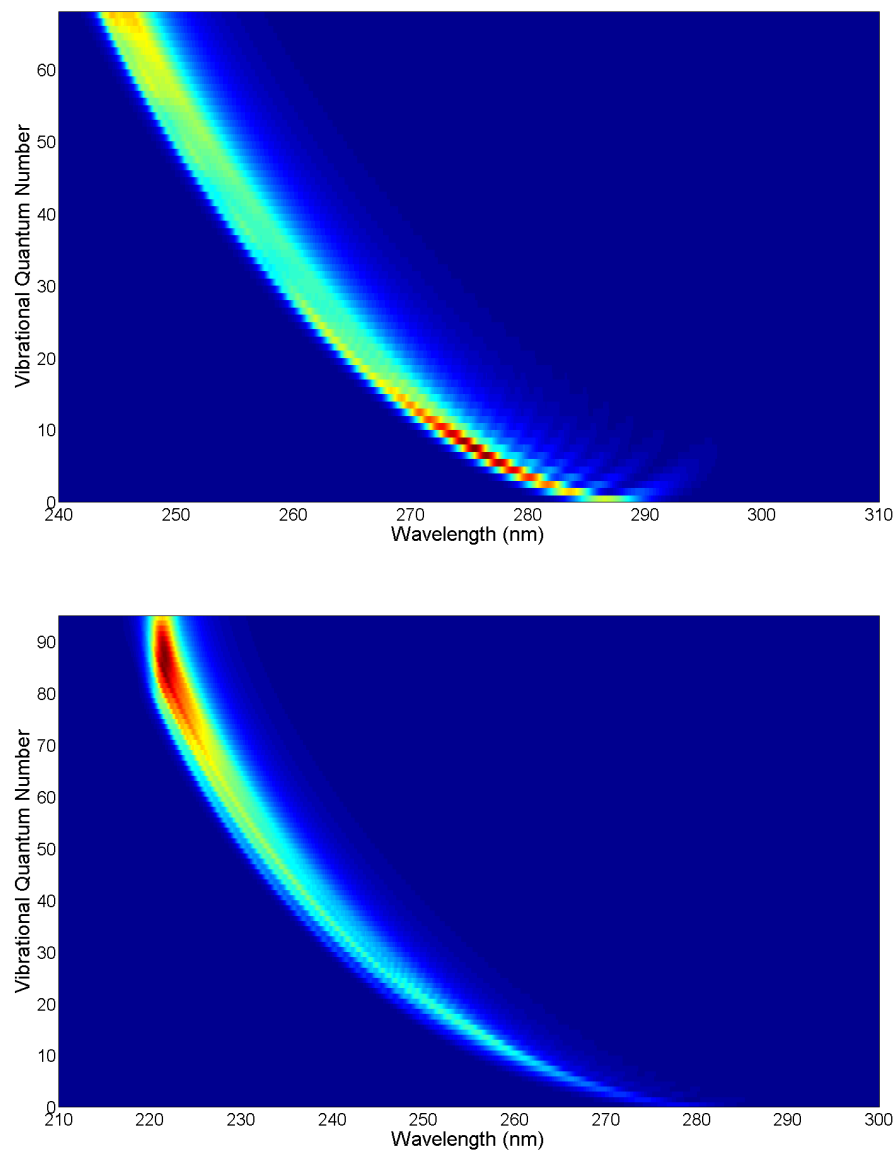


Figure 3.2: The relative population of various vibrational states vs. pumping wavelength. Red represents a higher relative population, while blue areas have less population. The cadmium (top) simulation was performed at 982 K and the zinc (bottom) simulation at 1118 K.

3.3 Net Gain Spectra

In the previous fluorescence simulations, it was assumed that all emission occurred from a single vibrational level. As should be apparent from the last section, even monochromatic excitation will create a distribution of upper state vibrational levels. For these simulations, the absorption is first simulated to find the distribution of upper state levels excited by the pumping source. Then, emission is calculated by weighting the upper state levels with their relative populations. The absorption spectrum is then subtracted from the emission spectrum. Each spectrum is weighted by an assumed inversion level. Net gain spectra produced with this method can be seen in Figures 3.3 and 3.4.

3.4 Validation

Before this particular code could be used for analysis, its accuracy had to be confirmed. There are several potentials for which an exact solution to the Schrodinger equation exists. These potentials include the free particle, the linear potential, the harmonic oscillator, and the Morse potential. The function used to find the free potentials, *Free_Wvfn_NC*, was tested by having it calculate the wavefunctions all four of these potentials and comparing it with the analytic solution. The function *Bound_Wvfn_Mat* was validated by showing that it produced the correct wavefunctions and energies for the harmonic oscillator and Morse potential. Finally, the entire simulation program was tested by reproducing the bound-free emission spectrum of Cs_2 [10], calculated by another group.

3.5 Optimization of Potentials

Up to this point in the chapter, only the forward model has been discussed. That is, given internuclear potential functions, how can the emission spectra be calculated? However, in the lab, we are confronted with the inverse problem: the emission spectra can be measured, but the internuclear potentials cannot. Due to the complexity of the forward model, the potentials cannot

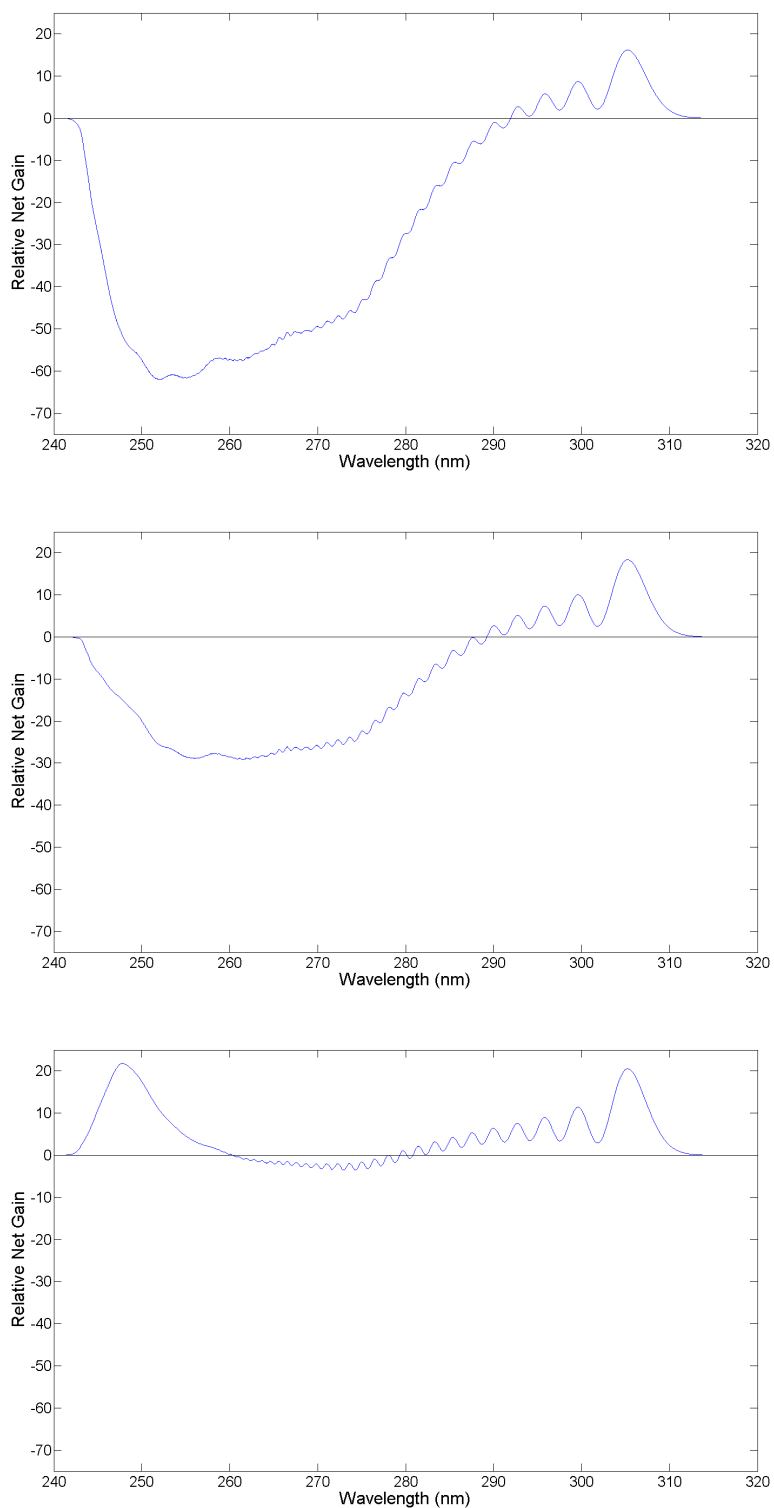


Figure 3.3: Simulated net gain spectra of cadmium assuming 75% (top), 85% (center), and 95% (bottom) of the population in the upper state. Note the significant loss of gain bandwidth as a smaller fraction of cadmium molecules occupy the upper state.

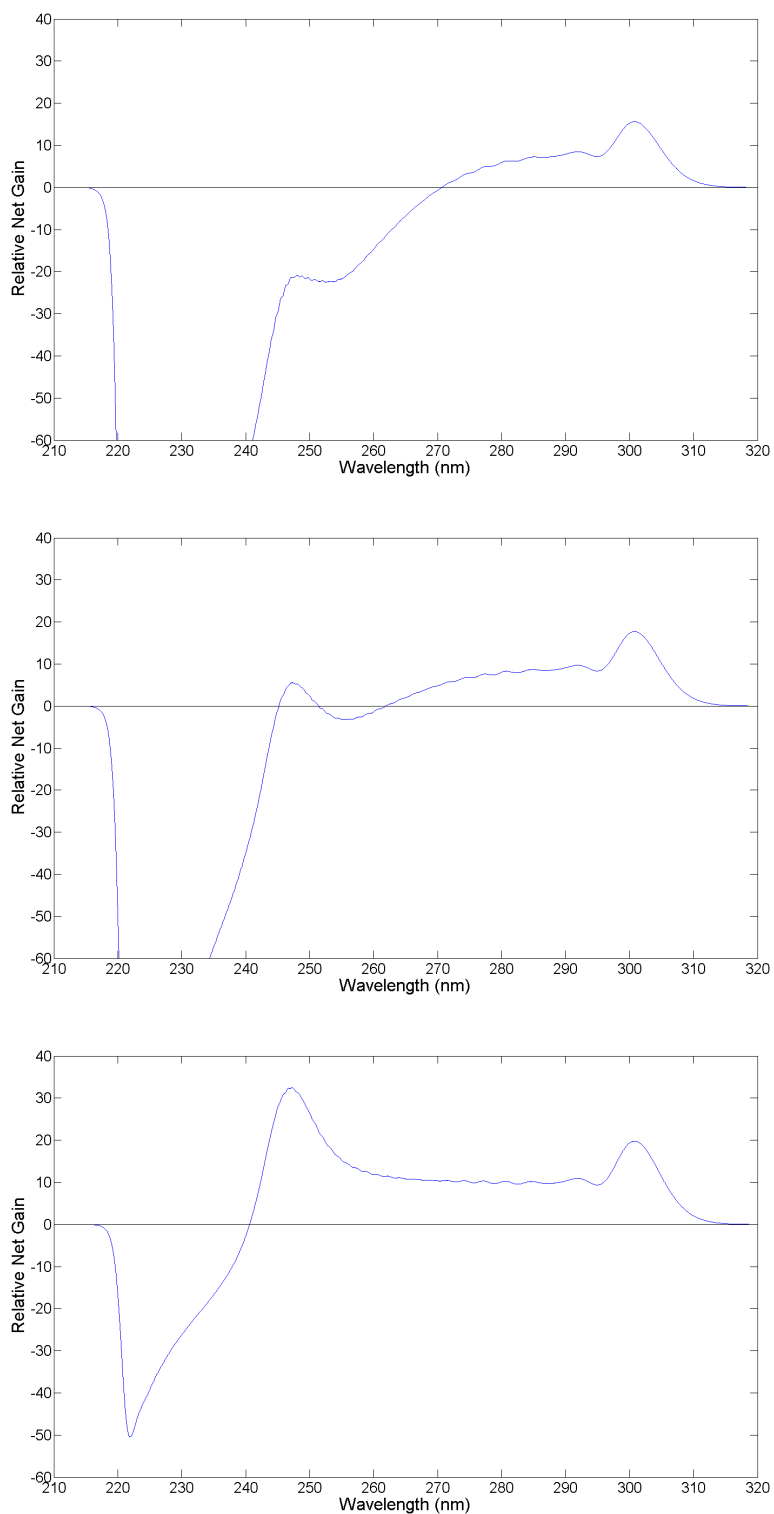


Figure 3.4: Simulated net gain spectra of zinc assuming 75% (top), 85% (center), and 95% (bottom) of the population in the upper state. Note the significant loss of gain bandwidth as a smaller fraction of zinc molecules occupy the upper state.

be easily inverted. The method of simulated annealing was used to optimize the functions being fit to that data.

The first step in attempting to model the internuclear potentials was to choose a functional form for the potential. The Morse potential was chosen to model both the upper and lower states because it has a simple structure. There are then four free parameters of the upper state: ω_e , $\omega_e x_e$, D_e , and R_e . Note that D_e is not technically a parameter of the Morse potential. It can be predicted from the equation [11]

$$D_e = \frac{\omega_e^2}{4\omega_e x_e} \quad (3.4)$$

However, the Morse potential is often a poor model near the dissociative limit. In this fit, the Morse potential is used only to model deeply-bound wavefunctions, where the behavior of the potential as it approaches the dissociated limit is irrelevant.

Simulated annealing is a method of multidimensional optimization. For to be used, a function of several variables which produces a scalar output is needed. The output scalar will be known as the “energy” and this quantity will be minimized. The algorithm is as follows: First the function is computed for a starting value. One of the parameters is then randomly altered and the function is recalculated. If the change decreases the simulated annealing energy (hereafter referred to as the ‘energy’), then it is accepted. However if the change increases the energy, it is accepted with a probability of $\exp(-\Delta E/T)$. Here T is a parameter of the algorithm known as the simulated annealing temperature. It can be shown that with this acceptance rule, the relative probability that the function will be at a given point is proportional to $\exp(-E)$.

As the simulation runs, the simulated annealing temperature is decreased, which will confine the solutions to only the lowest energy regions. In the limit that $T = 0$, simulated annealing becomes equivalent to the greedy algorithm. A finite temperature is needed so that trial moves will not get stuck at local minima but will instead be able to overcome local maxima.

The simulated annealing process must be manually tuned to approach an optimized solution efficiently. One value of importance to this tuning is the probability that a given move is accepted. This number is largely determined by the temperature and step size. If the acceptance rate is very close to unity,

Table 3.1: The optimized parameters specifying the upper state potential function for both cadmium and zinc excimers.

	ω_e (cm ⁻¹)	$\omega_e x_e$ (cm ⁻¹)	R_{eq} (Å)	D_e (cm ⁻¹)
Cadmium	92.28	0.2550	4.183	8074
Zinc	118.6	0.4063	3.568	9339

it is likely that very small moves are being taken. If the acceptance is low, then moves which are accepted will be large; but there will be very few of them. In either case, phase space is not efficiently explored.

The simulated annealing energy was defined to be the sum of the squares of the distances between the peaks from the measured spectrum and the calculated spectrum, which is a figure of merit describing how well the calculated spectrum fits the measured data with the given parameters. The parameters for this simulation were ω'_e , $\omega_e x'_e$, D'_e , and R'_e . Only the upper state potentials were optimized. The lower state potentials for both cadmium and zinc were taken from Czajkowski et al. [12], [13].

Simulated annealing was first performed to find potential functions which would result in the fluorescence spectra taken by Rodriguez and Eden in 1991 [14]. Spectra plotted in Rodriguez and Eden's paper was digitized from the paper because several of the pump sources they used were no longer available in the lab. Morse potential parameters for the upper state potentials of cadmium and zinc could not be optimized so that the resulting spectra reasonably matched all of the experimental data. This likely indicates that the full upper state potential cannot be accurately modeled with a Morse potential. For a single pump wavelength, however, a Morse potential can be a reasonable approximation. Potentials were fit to match the 248 nm fluorescence data only, because that pump wavelength is used in the current experiments.

The optimized parameters are given in Table 3.1 and the optimized spectra are shown in Figure 3.5. The cadmium spectrum appears to be well-optimized, while the zinc spectrum does not match the experimental data as closely. All of the simulations in this chapter used the fit parameters determined here. Because the optimized potentials do not match all observed data, the simulations presented in this chapter should not be considered

quantitatively accurate. However, they do qualitatively show the behavior of cadmium and zinc excimers.

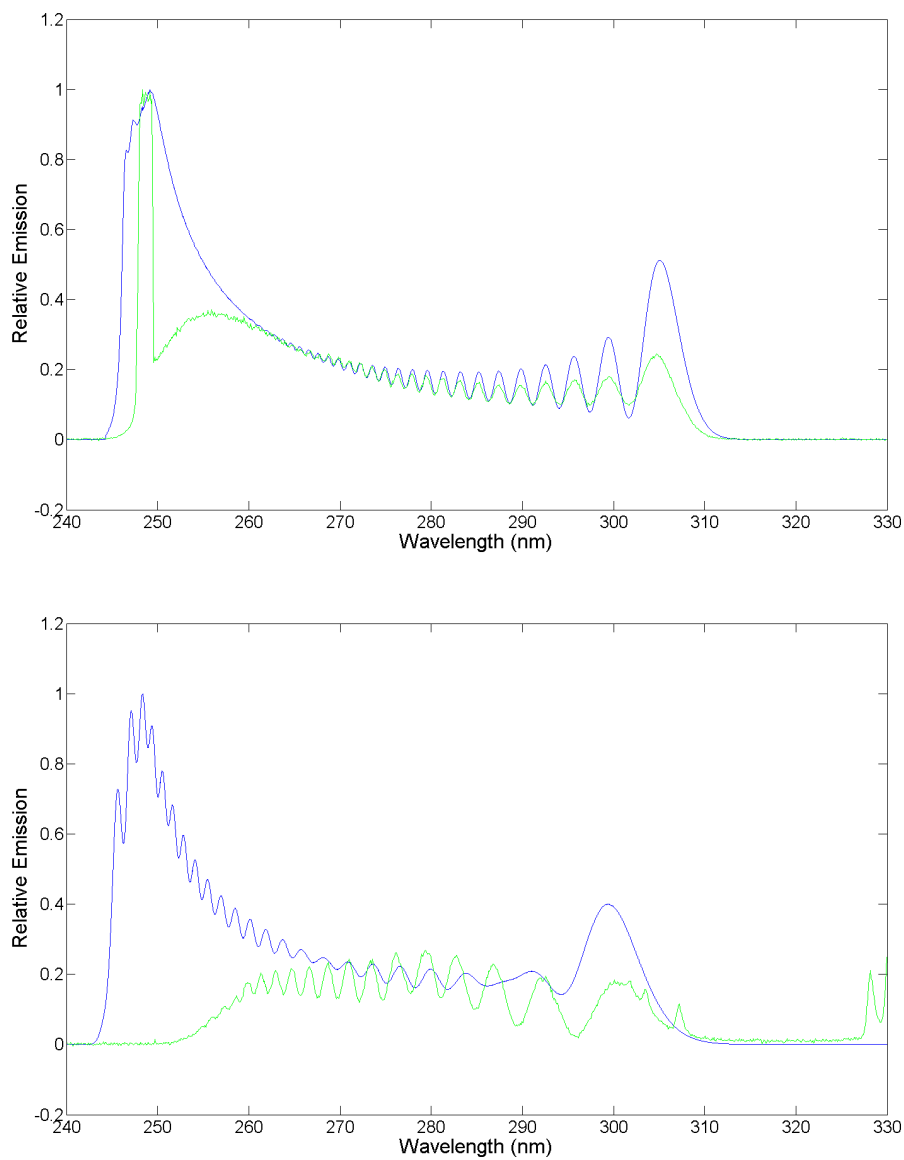


Figure 3.5: Simulated bound-free fluorescence spectra of cadmium (top) and zinc (bottom). The potentials used to generate these plots were optimized with simulated annealing. Experimental spectra are shown in green.

CHAPTER 4

EXPERIMENTS

In this chapter, experiments designed to aid in modelling and to demonstrate amplification are described.

4.1 Fluorescence Spectroscopy Experiments

The first step in the experiments was to reproduce the results of the 1991 fluorescence experiments performed by Rodriguez and Eden [14]. All of the new experiments described in this chapter used the original cadmium and zinc cells from Rodriguez and Eden's 1991 experiments. Reproducing the results would serve to demonstrate that the cells had not degraded over the past 18 years. To pump the cells, a Lambda Physik LPX 105 NT excimer laser was converted from argon fluoride to krypton fluoride by replacing the high reflecting mirror and changing the gas mixture. In this configuration, the laser produced 250-330 mJ per pulse, depending on the repetition rate.

An oven capable of producing temperatures up to 1400 K was constructed to heat the cells. As shown in Figure 4.1, the oven had two holes cut in the ends to allow a femtosecond laser beam to pass through it. Another hole was cut in the side for a pump laser. To ensure maximum power coupling into the cell, no windows were used. Sophisticated spectroscopic experiments often have a two-zone temperature controller for their cells. The area of lower temperature acts as a point of condensation, thus controlling the pressure of the cell. The zone of higher temperature controls the thermal distribution of the gas. To allow the experiment to be carried out quickly, the oven was constructed with only one zone of temperature control. Thus temperature and pressure could not be controlled independently. A thermocouple rested directly against the cell during all the experiments. After each experiment was completed and the cell under test had cooled, an inspection of the cell

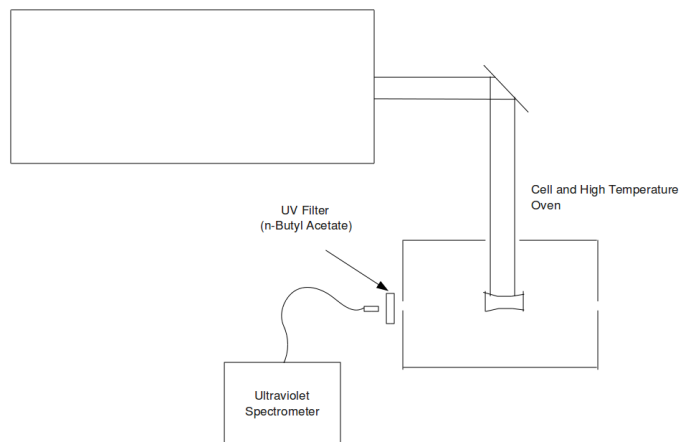


Figure 4.1: The experimental setup for the laser-induced fluorescence experiments.

showed that cadmium or zinc was always condensed inside the glass near the thermocouple. Thus it was inferred that the portion of the cell around the thermocouple represented the coolest part of the cell. Hence the pressure of the cell could be inferred from the reading of the thermocouple.

The setup for the fluorescence experiments is shown in Figure 4.1. The cells were side-pumped with 248 nm pulses from the aforementioned KrF laser. Spectra were measured with an Ocean Optics 4000 UV spectrometer observing fluorescence perpendicular to the pump. A background scan was recorded before every data scan so that blackbody radiation from the oven and other scattered light could be subtracted from the spectra. Noise in the spectra was cut by integrating the signal for 500 KrF pulses. To stop scattered pump radiation from damaging the spectrometer, an n-butyl acetate filter was placed between the oven and the spectrometer. This filter has a sharp transition from being strongly absorbing at 248 nm to being strongly transmissive at 253 nm. The spectra discussed below have not been corrected from the effects of the filter.

Results from this experiment can be seen in Figure 4.2. These spectra resemble those measured in 1991. Note that in the cadmium spectra shorter wavelengths are suppressed at high temperatures. This effect is due to the

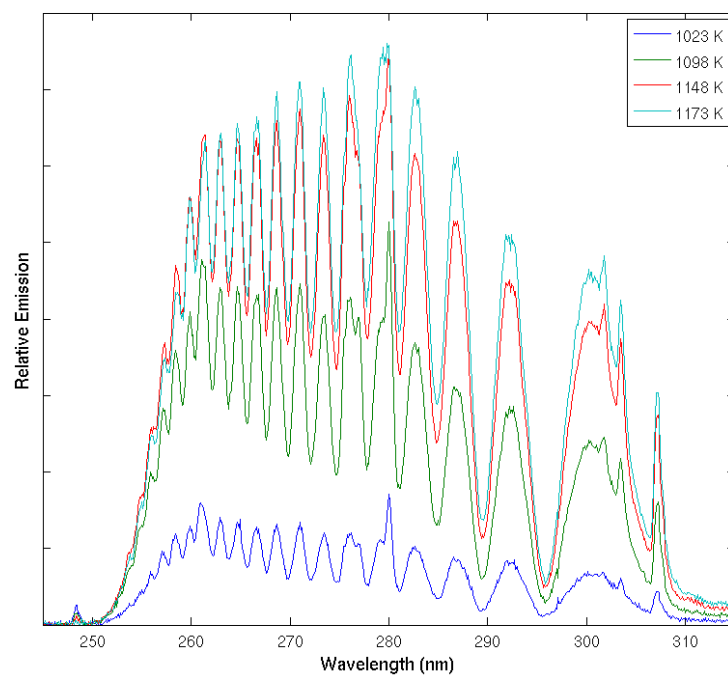
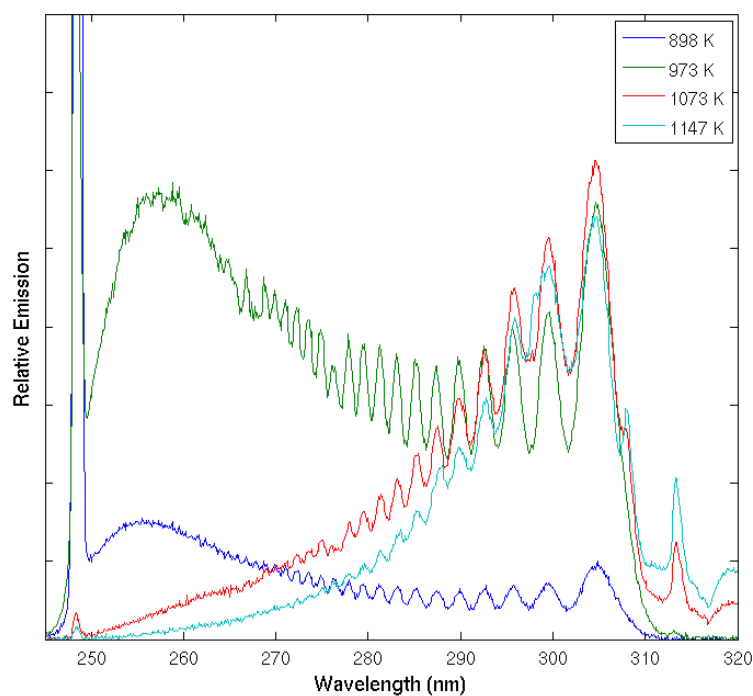


Figure 4.2: (Above) Fluorescence spectra of cadmium at several temperatures. Note the suppression of the shorter wavelengths at higher pressures. (Below) Fluorescence spectra of zinc at several temperatures. Note how, in contrast to cadmium, shorter wavelengths are not suppressed at higher temperatures.

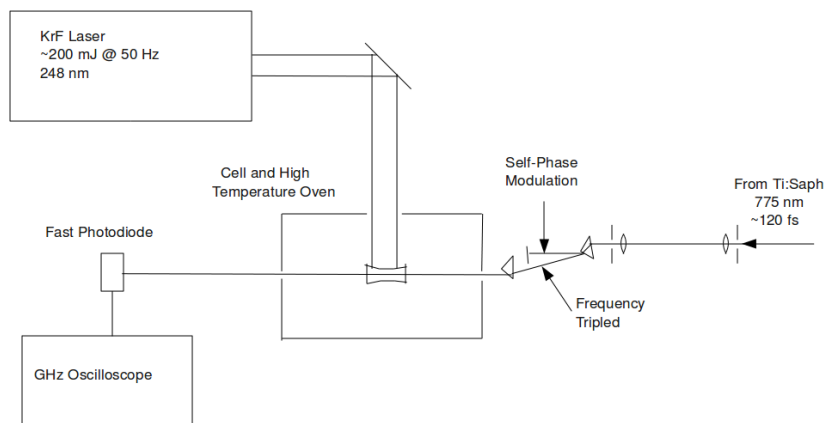


Figure 4.3: Experimental setup for the first attempt to demonstrate gain. The first lens focused the femtosecond beam to create a plasma in which a portion of the laser energy was frequency-tripled. The two apertures were used for alignment.

increased number density of cadmium atoms causing photons emitted at shorter wavelengths to be reabsorbed. A similar effect has been seen previously [9]. No such effect was seen in zinc. In general, cadmium absorbed more of the pump than zinc at a given number density. The zinc and cadmium cells are not exactly the same shape. In addition, the precise alignment of the laser, cell, and spectrometer could not be guaranteed every time. Hence the amplitudes of the fluorescence features cannot be compared directly.

4.2 Amplifier Experiments

The next step was to attempt to demonstrate gain in one of the cells. Because cadmium had shown stronger interaction with the pump beam, it was chosen for this experiment. The original plan was to use a femtosecond laser and an optical parametric amplifier (OPA) for this purpose. However, after a month of working on the OPA, it was apparent that it was not stable enough

to take reliable data. Instead, the femtosecond beam was frequency-tripled by focusing it in air. One drawback of this method was that the femtosecond laser was not easily tunable and could not be tuned above 780 nm (260 nm tripled). Additionally, this process also produced a strong background of self-phase modulation (SPM). The tripled portion of the beam was separated from the SPM by the use of two prisms and beam blocks. Only the tripled portion of the beam passed through the cell. The light was then collected with a UV photodiode or examined with a spectrometer. The setup for this experiment is shown in Figure 4.3.

It should also be noted that the femtosecond laser has a repetition rate of 1 kHz, while the excimer has a maximum rate of 50 Hz. A synchronization signal emitted by the femtosecond laser was used to trigger a digital delay generator, which in turn triggered the excimer and other electronics. Temporal alignment of the two beams was accomplished by placing a fast photodiode close to the oven where it could detect both the pump and seed beams. Actual data was taken with the photodiode far away from the oven to minimize signal from the scattered pump. The trigger time of the excimer was swept with the digital delay generator in order to optimize temporal alignment of the pulses. For measurements with the photodiode, it was possible to observe only the femtosecond pulses which traversed the cell while it was being pumped. However, the Ocean Optics spectrometer could not easily be gated to measure only the spectra while the medium was being pumped. Any changes in the observed spectrum would be relatively small because only 1 out of every 20 pulses seen by the spectrometer traversed a pumped medium.

The data from this experiment was initially confusing. The integrated height of the photodiode signal showed no apparent difference whether the pump beam was blocked or unblocked at each temperature. However, when the components were spectrally resolved, the tripled femtosecond beam appeared to grow significantly (by a factor of 40). This effect increased with increasing temperature.

A subsequent, more careful experiment showed that the ‘gain’ was not in fact caused by stimulated emission. In the new experiment, attention was paid to the absolute value of the signal transmitted through the cell. The data clearly showed that the power making it through the cell monotonically decreased with increasing temperature. The following mechanism has been

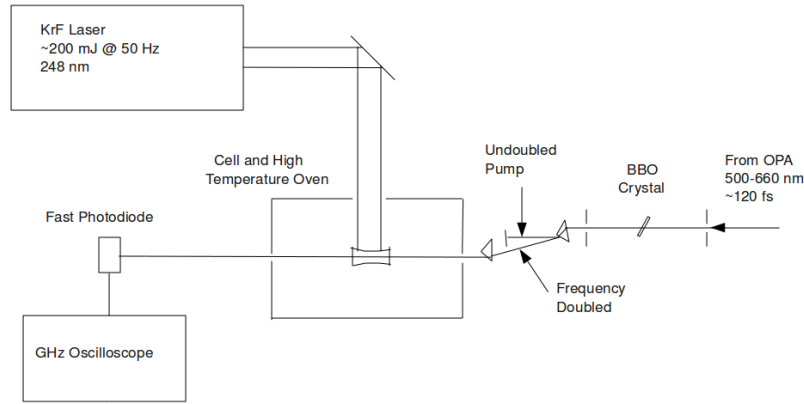


Figure 4.4: The current beam path of this experiment. This configuration has yet to produce data.

proposed to explain the results: The pump beam was focused into the cell and hence heated the center of the cell more than the edges. The increased heat reduced the density of atoms in the central region. As a result of the lower density, absorption decreased. The pump beam therefore simply modulated the absorption. No net gain was observed at 260 nm.

The results of this experiment were not discouraging. The 260 nm signal was too close to the pump wavelength. Photons emitted in that range are reabsorbed by neighboring zinc or cadmium pairs before they can escape the cell, just as we had seen in the fluorescence spectra. Subsequent modelling showed that absorption was strong in the region of 260 nm. The simulations show that gain is most likely to be demonstrated above 300 nm, where absorption is low.

The lab has acquired a new femtosecond laser and OPA which will make performing this experiment significantly easier. With this OPA it will be possible to tune the center frequency electronically. The OPA will be tuned to 500 - 660 nm and frequency doubled with a nonlinear beta barium borate (BBO) crystal. The remaining undoubled pump will be separated from the

probe beam with a prism pair. The signal will again be measured with either a spectrometer or fast photodiode. This experimental setup is shown in Figure 4.4

CHAPTER 5

CONCLUSION AND FUTURE WORK

While gain has not yet been demonstrated in cadmium or zinc, progress has been made in theoretically predicting the gain spectrum of these metal vapors. Net gain simulations predict a substantial gain bandwidth for even limited population inversions. The upper state potentials of diatomic cadmium and zinc have been reoptimized.

After gain is demonstrated in cadmium or zinc, there are a few experiments of immediate interest. The easiest to try would be to map out the gain spectra by tuning the optical parametric amplifier. It would also be of interest to measure the pulse duration after amplification. The lab's usual tool for performing such measurements, the FROG (Frequency Resolved Optical Grating) does not operate at UV wavelengths. This measurement would therefore have to be performed by setting up an optical autocorrelator. If those results are promising, the design of a more sophisticated setup will be considered.

There are two more interesting simulations to be performed. The gain spectrum will show what happens to a femtosecond pulse spectrally as it traverses the system, but also of interest is what happens to the pulse temporally. This simulation would involve backing out the real part of the index of refraction from the gain using the Kramers-Kronig relations.

APPENDIX A

SPECTRAL SIMULATION CODE

The code used to generate absorption, emission, and net gain spectra is available in the supplemental file **SourceCode.zip**. The code was originally developed by Thomas M. Spinka. It was later optimized (and, in cases, completely rewritten) by the author of this thesis.

At the time of this writing, the code will produce a new simulated spectra in around 30 seconds. Various optimizations allowed it to produce a new spectra in about 5 seconds when upper state potentials were being recalculated but lower state potentials were unchanged. Because these optimizations reduce the clarity and generality of the code, they have been commented or removed from the code in the supplementary file.

APPENDIX B

THE NUMEROV METHOD

The Numerov method [15] is a way to numerically integrate differential equations of the following form:

$$\left(\frac{d^2}{dx^2} + f(x)\right)y(x) = 0 \quad (\text{B.1})$$

If the x axis is divided into intervals length h , then the following recursion relation can be established for y :

$$y_{n+1} = \frac{\left(2 - \frac{5h^2}{6}f_n\right)y_n - \left(1 + \frac{h^2}{12}f_{n-1}\right)y_{n-1}}{1 + \frac{h^2}{12}f_{n+1}} \quad (\text{B.2})$$

The Schroedinger equation fits the form of Equation B.1. To see this, make the identifications:

$$y(x) = \psi(x) \quad (\text{B.3})$$

and

$$f(x) = \frac{2\mu}{\hbar^2}(E - V(x)) - \frac{l(l+1)}{x^2} \quad (\text{B.4})$$

There are some subtleties to consider when applying this method while integrating the Schroedinger equation. For this discussion, let the classically allowed region be $x_L < x < x_H$ and assume that the integration is carried out in the direction of increasing x . In the region $x < x_L$, the wavefunction is increasing at least exponentially. If the integration is started too far in the classically forbidden region, then it will overflow the floating point registers. This problem can be solved by renormalizing the wavefunction every time its amplitude increases beyond a given threshold. There is a similar complication if the Numerov method is used to find a bound wavefunction with a known energy. If the integration is carried out completely outwardly, then numerical error will cause the wavefunction to couple the exponentially growing solution

to the wave equation in the right classically forbidden region. As a result, the amplitude will diverge. This problem can be solved by integrating from the left and right simultaneously and normalizing each solution so they are equal where they meet.

REFERENCES

- [1] C. K. Rhodes, “Multiphoton ionization of atoms,” *Science*, vol. 229, pp. 1345–1351, Sept 1985.
- [2] U. Teubner, I. Uschmann, P. Gibbon, D. Altenbernd, E. Förster, T. Feurer, W. Theobald, R. Sauerbrey, G. Hirst, M. H. Key, J. Lister, and D. Neely, “Absorption and hot electron production by high intensity femtosecond uv-laser pulses in solid targets,” *Phys. Rev. E*, vol. 54, no. 4, pp. 4167–4177, Oct 1996.
- [3] S. Szatmari, G. Marowsky, and P. Simon, “Femtosecond excimer lasers and their applications,” in *Gas Lasers*, ser. Laser Systems, G. Herziger, H. Weber, and R. Poprawe, Eds. New York: Springer-Verlag, 2007, vol. 11, ch. 3.3, pp. 215–253.
- [4] E. W. Smith, R. E. Drullinger, M. M. Hessel, and J. Cooper, “A theoretical analysis of mercury molecules,” *The Journal of Chemical Physics*, vol. 66, no. 12, pp. 5667–5681, 1977. [Online]. Available: <http://link.aip.org/link/?JCP/66/5667/1>
- [5] M. A. Bubinskii, K. L. Schepler, R. Y. Abdulsabirov, and S. L. Korabl-eva, “All solid-state injection-seeded tunable ultraviolet laser,” *Journal of Modern Optics*, vol. 45, no. 10, pp. 1993–1998, May 1998.
- [6] C. D. Marshall, J. A. Speth, S. A. Payne, W. F. Krupke, G. J. Quarles, V. Castillo, and B. H. T. Chai, “Ultraviolet laser emission properties of Ce^{3+} -doped LiSrAlF_6 and LiCaAlF_6 ,” *J. Opt. Soc. Am. B*, vol. 11, no. 10, pp. 2054–2065, 1994. [Online]. Available: <http://josab.osa.org/abstract.cfm?URI=josab-11-10-2054>
- [7] C. F. Bender, T. N. Rescigno, H. F. Schaefer III, and A. E. Orel, “Potential energy curves for diatomic zinc and cadmium,” *The Journal of Chemical Physics*, vol. 71, no. 3, pp. 1122–1127, 1979. [Online]. Available: <http://link.aip.org/link/?JCP/71/1122/1>
- [8] J. Tellinghuisen, “The Franck–Condon principle in bound-free transitions,” in *Photodissociation and Photoionization*, ser. Advances in Chemical Physics, K. P. Lawley, Ed. New York: John Wiley and Sons, 1985, vol. LX, ch. 7, pp. 299–369.

- [9] D. J. Ehrlich and R. M. Osgood, “Condon internal diffraction in the $o_u^+ \rightarrow o_g^+$ fluorescence of photoassociated Hg_2 ,” *Phys. Rev. Lett.*, vol. 41, no. 8, pp. 547–550, Aug 1978.
- [10] J. Tellinghuisen, “Reflection and interference structure in diatomic Franck–Condon distributions,” *Journal of Molecular Spectroscopy*, vol. 103, pp. 455–465, 1984.
- [11] G. Herzberg, *Molecular Spectra and Molecular Structure*, 2nd ed. Princeton, NJ: D. Van Nostrand Company, Ltd., 1950, vol. 1.
- [12] M. Czajkowski, R. Bobkowski, and L. Krause, “ $\text{O}_u^+ ({}^3\Pi_u) \leftarrow \text{XO}_g^+ ({}^1\Sigma_g^+)$ transitions in Zn_2 excited in crossed molecular and laser beams,” *Phys. Rev. A*, vol. 41, no. 1, pp. 277–282, Jan 1990.
- [13] M. Czajkowski, R. Bobkowski, and L. Krause, “ $\text{O}_u^+ ({}^3\Pi_u) \leftarrow \text{XO}_g^+ ({}^1\Sigma_g^+)$ transitions in Cd_2 excited in crossed molecular and laser beams,” *Phys. Rev. A*, vol. 40, no. 8, pp. 4338–4343, Oct 1989.
- [14] G. Rodriguez and J. G. Eden, “Bound→free emission spectra and photoassociation of ${}^{114}\text{Cd}_2$ and ${}^{64}\text{Zn}_2$,” *The Journal of Chemical Physics*, vol. 95, no. 8, pp. 5539–5552, 1991. [Online]. Available: <http://link.aip.org/link/?JCP/95/5539/1>
- [15] E. Hairer, *Solving Ordinary Differential Equations I: Nonstiff Problems*, 2nd ed. Berlin: Springer-Verlag, 1993, vol. 1.